doi:10.1016/j.jmb.2005.05.059 J. Mol. Biol. (2005) 351, 355–370

JMB

Available online at www.sciencedirect.com

SCIENCE DIRECT®

ELSEVIER

Structure of the Terminal Oxygenase Component of Angular Dioxygenase, Carbazole 1,9a-Dioxygenase

Hideaki Nojiri[1,2*†], Yuji Ashikawa[1†], Haruko Noguchi[1,2] Jeong-Won Nam[1], Masaaki Urata[1], Zui Fujimoto[3], Hiromasa Uchimura[1] Tohru Terada[2], Shugo Nakamura[2,4], Kentaro Shimizu[2,4] Takako Yoshida[1], Hiroshi Habe[1] and Toshio Omori[1]

[1]*Biotechnology Research Center The University of Tokyo, 1-1-1 Yayoi, Bunkyo-ku, Tokyo 113-8657, Japan*

[2]*Professional Programme for Agricultural Bioinformatics The University of Tokyo, 1-1-1 Yayoi, Bunkyo-ku, Tokyo 113-8657, Japan*

[3]*Department of Biochemistry National Institute of Agrobiological Sciences, 2-1-2 Kannondai, Tsukuba, Ibaraki 305-8602, Japan*

[4]*Department of Biotechnology The University of Tokyo, 1-1-1 Yayoi, Bunkyo-ku, Tokyo 113-8657, Japan*

**Corresponding author*

Carbazole 1,9a-dioxygenase (CARDO) catalyzes the dihydroxylation of carbazole by angular position (C9a) carbon bonding to the imino nitrogen and its adjacent C1 carbon. This reaction is an initial degradation reaction of the carbazole degradation pathway by various bacterial strains. Only a limited number of Rieske non-heme iron oxygenase systems (ROSs) can catalyze this novel reaction, termed angular dioxygenation. Angular dioxygenation is also involved in the degradation pathways of carbazole-related compounds, dioxin, and CARDO can catalyze the angular dioxygenation for dioxin. CARDO consists of a terminal oxygenase component (CARDO-O), and the electron transport components, ferredoxin (CARDO-F) and ferredoxin reductase (CARDO-R). CARDO-O has a homotrimeric structure, and governs the substrate specificity of CARDO. Here, we have determined the crystal structure of CARDO-O of *Janthinobacterium* sp. strain J3 at a resolution of 1.95 Å. The α_3 trimeric overall structure of the CARDO-O molecule roughly corresponds to the α_3 partial structures of other terminal oxygenase components of ROSs that have the $\alpha_3\beta_3$ configuration. The CARDO-O structure is a first example of the terminal oxygenase components of ROSs that have the α_3 configuration, and revealed the presence of the specific loops that interact with a neighboring subunit, which is proposed to be indispensable for stable α_3 interactions without structural β subunits. The shape of the substrate-binding pocket of CARDO-O is markedly different from those of other oxygenase components involved in naphthalene and biphenyl degradation pathways. Docking simulations suggested that carbazole binds to the substrate-binding pocket in a manner suitable for catalysis of angular dioxygenation.

Keywords: angular dioxygenation; carbazole 1,9a-dioxygenase; Rieske non-heme iron oxygenase systems; biodegradation; Rieske-type protein

Introduction

Carbazole (CAR) is the predominant *N*-heterocyclic aromatic compound in coal tar creosote, and is a recalcitrant molecule with mutagenic and toxic activities.[1] To achieve remediation of creosote-contaminated soil, bacterial degradation of CAR has been studied as reviewed by Nojiri & Omori.[2]

† H.N. & Y.A. contributed equally to this work.

Present address: Toshio Omori, Department of Industrial Chemistry, Shibaura Institute of Technology, 3-9-14 Shibaura, Minato-ku, Tokyo 108-8548, Japan.

Abbreviations used: a.a., amino acid; BDO, biphenyl 2,3-dioxygenase; CAR, carbazole; CARDO, carbazole 1,9a-dioxygenase; CARDO-F, ferredoxin component of carbazole 1,9a-dioxygenase; CARDO-O, terminal oxygenase component of carbazole 1,9a-dioxygenase; CARDO-R, ferredoxin reductase component of carbazole 1,9a-dioxygenase; CDO, cumene 2,3-dioxygenase; MAD, multiple-wavelength anomalous dispersion; NDO, naphthalene 1,2-dioxygenase; ROSs, Rieske non-heme iron oxygenase systems.

E-mail address of the corresponding author: anojiri@mail.ecc.u-tokyo.ac.jp

0022-2836/$ - see front matter

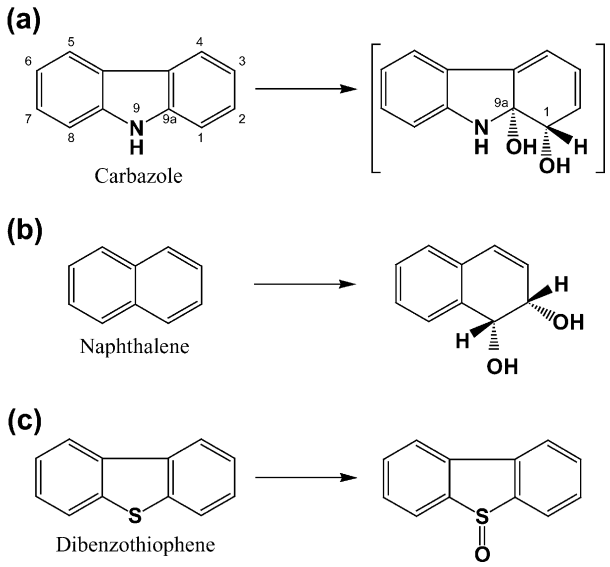

Figure 1. Oxygenations catalyzed by CARDO isolated from various bacteria. Angular dioxygenation of CAR (a) involves the addition of two hydroxyl groups with the *cis*-configuration at the angular position, to yield the unstable intermediates shown in parentheses. CARDO also catalyzes lateral dioxygenation of naphthalene (b) to yield *cis*-dihydrodiols of the parental substrate. For dibenzothiophene (c), CARDO catalyzes monooxygenation of a sulfur atom, while it also catalyzes lateral dioxygenation of this substrate.

We have investigated extensively the degradation reactions, the degradative enzymes, and the degradation genes for CAR of *Pseudomonas resinovorans* strain CA10. As shown in Figure 1(a), CAR is initially dioxygenated at the C9a carbon, which is bonded to the nitrogen atom (termed the angular position), and its adjacent C1 carbon. This initial reaction, which is termed angular dioxygenation, is known to be involved in the degradation pathways of several aromatic compounds with similar structures, such as CAR, dioxin, and fluorene.[2] This novel reaction is catalyzed by some of the multicomponent-type Rieske non-heme iron oxygenase systems (ROSs), which are designated specifically as angular dioxygenases. The angular dioxygenase for CAR, CAR 1,9a-dioxygenase (CARDO), consists of a terminal oxygenase and electron transport proteins.[3,4] The terminal oxygenase of CARDO, which hereinafter will be simply referred to as CARDO-O, is a homotrimeric enzyme that contains one Rieske [2Fe-2S] cluster (hereinafter referred to simply as a Rieske cluster) and one active site iron (Fe^{2+}) in a single subunit (CarAa). The electron transport proteins of CARDO, which mediate electron transport from NAD(P)H to CARDO-O, comprise ferredoxin (CARDO-F; a monomer of CarAc), which contains one Rieske cluster, and ferredoxin reductase (CARDO-R; a monomer of CarAd), which contains one FAD and one plant-type [2Fe-2S] cluster.[3,4] Angular dioxygenation of CAR yields an unstable *cis*-hydrodiol (shown in brackets in Figure 1(a)), which is spontaneously converted to 2′-aminobiphenyl-2,3-diol.

With very few exceptions, ROSs catalyze the incorporation of both oxygen atoms of molecular dioxygen to tandemly linked carbon atoms on an aromatic ring as two hydroxyl groups in the *cis*-configuration. As distinct from angular dioxygenation, this type of dioxygenation is called lateral dioxygenation. For example, the lateral dioxygenation of naphthalene is shown in Figure 1(b). In addition to lateral dioxygenation, several ROSs have been reported to catalyze another type of oxygenation. Thus, naphthalene 1,2-dioxygenase (NDO) of *Pseudomonas* sp. strain NCIB9816-4 can catalyze lateral dioxygenation, monooxygenation (including sulfoxidation), desaturation, and dealkylation.[5] CARDO has also been shown to catalyze diverse oxygenation reactions within a broad substrate range, including angular dioxygenation, lateral dioxygenation, and monooxygenation (Figure 1).[6] Although numerous ROSs have been isolated and characterized to date, only a limited number of these can catalyze angular dioxygenation.

CARDO-O can also catalyze angular dioxygenation to dibenzofuran and dibenzo-*p*-dioxin, which are the parental compounds of dioxins.[6] In the remediation of dioxin contamination, angular dioxygenation represents an attractive and ideal reaction, as compared to other degradation reactions, since the former reaction forms an unstable hemiacetal intermediate that spontaneously converts the hetero ring-cleaved compound. In other words, single-step oxygenation leads to the destruction of the planar structure of dioxin, which determines its toxicity.[2] Thus, angular dioxygenases and the bacteria that express them could be important as tools for the remediation of dioxin contamination. However, since the increment of chlorine substitutions drastically decreases the oxygenation efficiency of CARDO-O, further improvements to increase the conversion rate to highly chlorinated dioxin congeners are needed.

ROSs have been classified into three major groups based on the number of constituent components and the nature of the redox center.[7] The characteristics of the electron transport chain suggest that CARDO should be classified as class III in Batie's classification.[4] However, phylogenetic analysis indicates that the amino acid (a.a.) sequence of the CARDO-O monomer (CarAa) shares rather low-level homology (<19% overall length-wise identity) with other known catalytic subunits of terminal oxygenases of ROSs. In addition, while typical class III ROSs contain the terminal oxygenase component that consists of both α and β subunits with the $\alpha_3\beta_3$ (or $\alpha_2\beta_2$) configuration, CARDO-O consists of only the catalytic (α) subunit with the α_3 configuration. This homomultimeric structure is typical of class IA ROSs, whose terminal oxygenases have reported to have α_2, α_3, α_4, or α_6 configurations.[8,9]

Considering these properties of the CARDO,

studies of substrate recognition, subunit assembly, and electron transport are of great interest. Although we have purified and partially characterized the respective components of CARDO,[4] the detailed mechanism underlying the catalysis of unique reactions has not been elucidated, owing to a lack of information on the three-dimensional structures of the CARDO components. Recently, we succeeded in solving the crystal structure of CARDO-F from *P. resinovorans* strain CA10.[10] As for CARDO-O, we have achieved the crystallization of the native form from strain CA10 (termed CARDO-O_{CA10} or $CarAa_{CA10}$), and preliminary X-ray diffraction data have been obtained.[11] To the best of our knowledge, the crystal structures of the terminal oxygenase components of NDO of *Pseudomonas* sp. strain NCIB9816-4 (NahAcAd)[12] and biphenyl 2,3-dioxygenase (BDO) of *Rhodococcus* sp. strain RHA1 (BphA1A2),[13] and cumene 2,3-dioxygenase (CDO) of *P. fluorescens* strain IP01 (CumA1A2),[14] have been reported (hereinafter these three will be referred to as NDO-O, BDO-O, and CDO-O, respectively). These terminal oxygenases have the $\alpha_3\beta_3$ configuration, and catalyze lateral dioxygenation as a primary reaction. Attempts to solve the CARDO-O structure by the molecular-replacement method using the NDO-O structure, have proven unsuccessful owing to the low homology (17.1% overall length-wise identity between the catalytic subunits CarAa and NahAc) and the structural differences expected from sequence alignments.

Here, we present the crystal structure of CARDO-O (CARDO-O_{J3}) from the CAR-degrader *Janthinobacterium* sp. strain J3,[15] which was obtained using multiple-wavelength anomalous dispersion (MAD) methods. This is the first report on the structure of the terminal oxygenase component of angular dioxygenase. In addition, the CARDO-O_{J3} structure is the first example of a terminal oxygenase component of ROSs with the α_3 composition.

Results and Discussion

Purification of histidine-tagged CARDO-O_{J3}

$CarAa_{J3}$, which is a subunit of CARDO-O_{J3}, contains 384 a.a. residues and is similar to $CarAa_{CA10}$, with only three a.a. mismatches. No functional differences have been observed between CARDO-O_{J3} and CARDO-O_{CA10} in terms of the substrate specificities (data not shown). Although the native (tagless) form was used in a previous crystallization study,[11] in the present study, the C-terminal His-tagged form of $CarAa_{J3}$ was expressed in *Escherichia coli* for rapid purification. Approximately 3–4 mg of His-tagged CARDO-O_{J3} was obtained routinely from one liter of SB medium culture.[4] The purified CARDO-O_{J3} was almost homogeneous on SDS-PAGE (data not shown). Gel-filtration analysis showed that CARDO-O_{J3} was trimeric, as was CARDO-O_{CA10} (data not shown). Before crystallization, the purified CARDO-O_{J3} was confirmed to have retained the angular dioxygenation activity for CAR when the purified electron transfer proteins CARDO-F_{CA10} and CARDO-R_{CA10} were supplied (data not shown).

Crystallography

Using the hanging-drop, vapor-diffusion method, the formation of red-brown square-shaped crystals of CARDO-O_{J3} (0.2 mm×0.2 mm×0.2 mm) was observed at 20 °C with a reservoir solution that comprised 15–17.5% methyl-pentane diol (MPD), 0.1 M Mes (pH 6.2), and 15–25 mg/ml of protein. The dissolved crystals of CARDO-O_{J3} retained about 80–90% of the angular dioxygenation activity for CAR of purified CARDO-O_{J3} (data not shown). Also, the iron content in the dissolved crystals was determined as 2.1(±0.5) mol/mol of monomeric protein, while that was determined as 2.3(±0.3) mol/mol just after the purification. These results clearly suggested that CARDO-O_{J3} exists as an active and native form in the crystals obtained. The diffraction data for these crystals were collected in a nitrogen stream at 100 K using the BL41XU station of SPring-8. Based on the results of the X-ray diffraction analysis, the crystals of CARDO-O_{J3} were assigned to the cubic space group $P2_13$ with unit cell parameters $a=b=c=131.9$ Å and diffracted to 1.95 Å resolution (Table 1).

The structure of CARDO-O was determined by the MAD technique, using a cubic crystal form of selenomethionine (SeMet)-substituted CARDO-O_{J3}. Once the phase of CARDO-O_{J3} in the SeMet-substituted crystal was determined at 2.3 Å resolution, the structure of the non-substituted CARDO-O_{J3} crystal was refined using the phase from the MAD data against the diffraction data with 1.95 Å spacing. The final refined model of CARDO-O_{J3} yielded a crystallographic R-factor of 19.4% and R_{free} factor of 20.5% (Table 1). The cubic crystal contained one subunit per asymmetric unit. One subunit in the final model contained 389 a.a. residues and 320 water molecules; the last three residues in the 6×His-tag were not observed. The quality of the present model was deemed to be good, and more than 88% of all the non-glycine and non-proline residues were in the most favorable region of the Ramachandran plot, with no residues in the disallowed region (data not shown).

Quaternary structure of CARDO-O

Gel-filtration analysis has demonstrated that CARDO-O_{J3} has the α_3 structure.[4] Based on our findings and the data on the crystal structures of NDO-O, BDO-O, and CDO-O,[12–14] we believe that the trimeric structure of the CARDO-O crystal exists on a crystallographic 3-fold axis, although the crystal contains one subunit per asymmetric unit.

Table 1. Crystal parameters, data collection statistics, and crystallographic refinement statistics

		Se-Met CARDO-O_{J3}		
Data set	CARDO-O_{J3}	Peak	Edge	Remote
A. *Crystal data*				
Wavelength (Å)	1.000	0.9794	0.9796	0.9820
Space group	$P2_13$	$P2_13$		
Cell parameter (Å)				
a	131.9	130.3		
b	131.9	130.3		
c	131.9	130.3		
Resolution (Å)[a]	15.00–1.95 (2.02–1.95)	53.5–2.30 (2.42–2.30)	64.6–2.30 (2.42–2.30)	55.0–2.30 (2.42–2.30)
No. of reflections				
Observed	307,722	278,892	261,035	296,029
Unique[a]	55,045 (5516)	32,897 (4784)	32,786 (4752)	35,657 (5,151)
Completeness (%)[a]	98.7 (100.0)	99.8 (99.8)	99.8 (99.8)	99.8 (99.8)
Multiplicity[a]	5.6	8.5 (8.6)	8.0 (7.2)	8.3 (8.2)
I/σ[a]	36.8 (4.5)	5.6 (2.3)	6.1 (2.3)	5.6 (2.7)
R_{merge} (%)[a]	0.060 (0.300)	0.102 (0.352)	0.100 (0.368)	0.102 (0.303)
B. *Refinement*				
Resolution (Å)	14.94–1.95 (2.02–1.95)			
R-factor (%)[b]	19.4 (24.8)			
R_{free} (%)[c]	20.5 (25.8)			
No. of protein atoms	3137			
No. of water molecules	320			
R.m.s. deviations				
Bond lengths (Å)	0.005			
Bond angles (°)	1.333			

[a] Values in parentheses are for the outermost shell.
[b] *R*-factor is defined as $R = \Sigma||F_{obs}| - |F_{calc}||/\Sigma|F_{obs}|$.
[c] R_{free} has been calculated using 5% of the unique reflections.

The overall shape of CARDO-O resembles that of a 100 Å wide doughnut, with a 30 Å hole and 45 Å thickness (Figure 2(a) and (b)). The monomeric structure in the asymmetric unit facilitates trimeric interactions with neighboring asymmetric units along the crystallographic 3-fold axis. The reported structure of the α-subunits of NDO-O is shown in Figure 2(c) and (d). Although there are some apparent differences, such as subunit size and the size of the centrally located hole, the subunit interactions in the CARDO-O roughly resemble those between the three α subunits of the hetero-hexameric NDO-O. Based on the mushroom-like overall structures of NDO-O, it seems likely that this type of structure is common among the terminal oxygenase components of class IB, II, and III ROSs with the $\alpha_3\beta_3$ configuration. Based on the crystal structure of CARDO-O (Figure 2(a) and (b)), the doughnut shape is likely to be the common and typical one for terminal oxygenase components in the class IA ROSs that have the α_3 configuration.

The subunit structure of CARDO-O

Each CARDO-O subunit contains the active site mononuclear iron and the Rieske cluster, and has 14 α-helices and 22 β-strands that are numbered consecutively (Figure 3(a) and (b)). The structure of the CARDO-O subunit can be divided into two distinct domains. The structure and the relative arrangement of the two domains are common among the α-subunits of previously solved terminal oxygenases of ROSs. In the CARDO-O structure, according to Kauppi *et al.*,[12] one domain has a Rieske cluster, which is termed the Rieske domain (residues 27–143), and the other domain, which contains non-heme iron at the active site, is termed the catalytic domain (residues 1–26 and 144–384).

The Rieske domain

The Rieske domain contains a Rieske cluster that is co-ordinated by Cys69, Cys90, His71, and His93. This domain consists of three separate antiparallel β-sheet structures (comprising 11 β-strands) that have been numbered β_1 sheet (β1, β10, and β11), β_2 sheet (β2-4), and β_3 sheet (β5-9), respectively (Figures 3(a) and 4(a)). The β_1 and β_2 sheets are arranged in a β-sandwich topology as distal and proximal sheets, respectively, to the Rieske cluster in a single subunit. Two-loop structure protrudes in a roughly perpendicular orientation with respect to the β_2 sheet, and forms two fingers with the Rieske cluster at their tips (Figure 4(a)). The first two iron ligands for the Rieske cluster are positioned in the loop between β4 and α4. The second pair of iron ligands for the cluster is found in the loop between β6 and β7 in the β_3 sheet. In the Rieske domain of the CARDO-O subunit, an additional long loop (107–119 a.a. residues) provides the third and final wall of the Rieske cluster. Although size varies among the related proteins (see the following section and Figure 4(b) and (c)), this additional long loop corresponds to the Pro loop in BphF, which is the ferredoxin component of BDO of *Burkholderia* sp. strain LB400 (hereinafter designated BDO-F).[16]

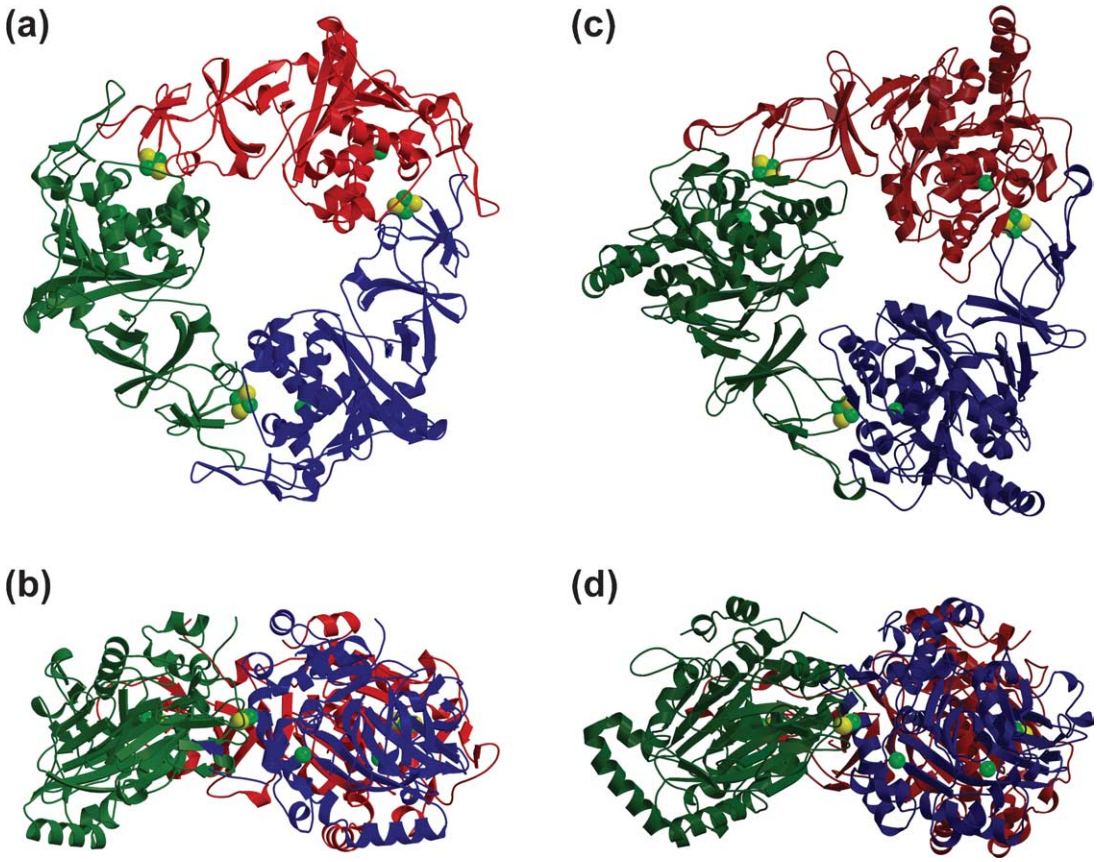

Figure 2. Comparison of the overall structures CARDO-O with the α subunits of NDO-O. Overall structures of CARDO-O ((a) and (b)) and the α subunits of NDO-O from *Pseudomonas* sp. strain NCIB9816-4 ((c) and (d)). Three subunits are colored by the combination of forest-green, blue, and red, or dark-green, dark-blue, and dark-red, respectively. The Rieske cluster and an active site iron are shown in the CPK model representation (iron and sulfide ions are shown in green and yellow, respectively). (a) and (c) The view along the molecular 3-fold axis. (b) and (d) Side-views of the trimer molecule shown in (a) and (c), respectively.

Comparison of the Rieske domain of CARDO-O with those of related proteins

The structure of the Rieske domain of the CARDO-O subunit has a fold that is similar to those of the corresponding parts of other related proteins. Superposition of the Rieske domain of the CARDO-O subunit onto the corresponding parts of NDO-O[12] and BDO-O[13] resulted in a root-mean-square difference (rmsd) of 4.3 Å (115 C^{α} atoms) and 4.1 Å (103 C^{α} atoms), respectively. However, there are two noteworthy differences between the Rieske domain structures of the three terminal oxygenases. The first difference is in the structures of the regions between the two loops that contain the ligands for the Rieske cluster (Figure 4(b), red arrow). In these regions, each oxygenase subunit has a single β strand, i.e. β5 in the CARDO-O subunit, β9 in the NDO-O α subunit, and β7 in the BDO-O α subunit. Since β5 of the CARDO-O monomer constitutes the β_3 sheet with β6 to β9 strands, the formed β_3 sheet is clearly distinct from the basal β-sandwich structure that is formed by the β_1 and β_2 sheets (Figure 4(a) and (b)). On the other hand, in the structures of NDO-O and BDO-O, the corresponding regions form a loop, which extends to the basal β-sandwich structure, and each β-strand in the region constitutes the β-sheet that corresponds to the β_2 sheet in the CARDO-O structure. Since, in the NDO-O and BDO-O structures, these long loops are involved in interactions with the respective β subunits (see the section entitled Interactions between the subunits), the above-mentioned difference may explain why CARDO-O consists of only three molecules of CarAa without β subunits. Additional differences between the Rieske domains are seen for the size and the position of the long loop that constitutes the third wall at the tip of the Rieske domain (Figure 4(b), blue arrow). The loops are more extensive in NDO-O and BDO-O than in CARDO-O. In the CARDO-O structure, β8 and β9, which are located at the stem region of a long loop, constitute the β_3 sheet with β5 to β7 strands. This is the reason why the position of the long loop is markedly different from those in NDO-O and BDO-O. From the NDO-O structure, the corresponding long loop is involved, to a large extent, in the interactions with the catalytic domain of the neighboring α subunit. Therefore, the difference in this region is considered to affect the interaction between the catalytic

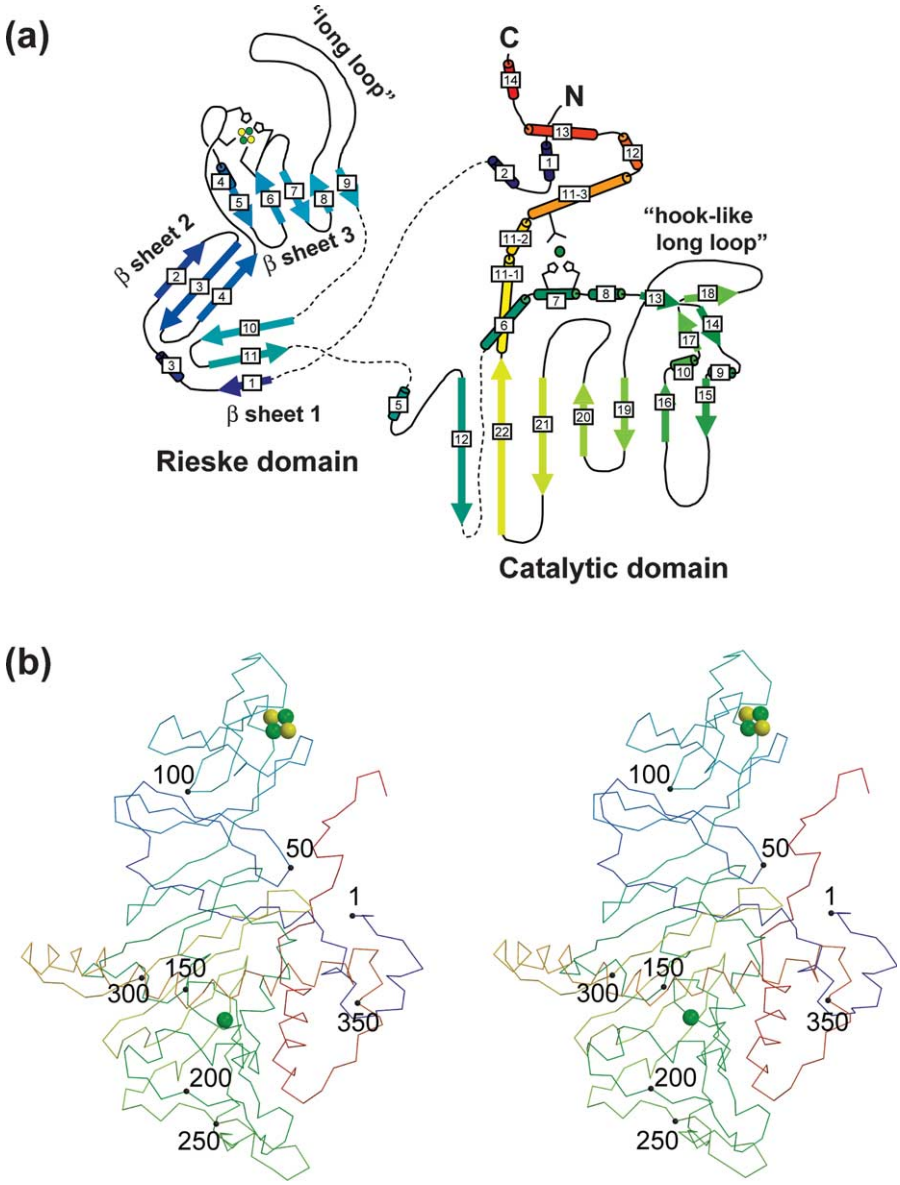

Figure 3. Structure of the CARDO-O monomer. (a) The secondary structure; α-helices are indicated by cylinders and β-strands are indicated by arrows. The α-helices and β-strands are color-ramped from blue at the N terminus to red at the C terminus. (b) Stereo diagram showing the flow of the chain. The iron and sulfide ions are shown as green and yellow spheres, respectively. The Rieske cluster and an active site iron are shown in a ball-and-stick representation. This diagram is color-ramped from blue at the N terminus to red at the C terminus.

subunits, which may correlate with the difference between the α_3 and $\alpha_3\beta_3$ configurations.

The crystal structures of the Rieske-type ferredoxins, BDO-F[16] and CARDO-F,[10] are currently available. The C^{α} folding of the entire Rieske domain of CARDO-O can be superimposed upon those of BDO-F and CARDO-F, with rmsd values of the C^{α} position of 4.3 Å (108 C^{α} atoms) and 4.9 Å (103 C^{α} atoms), respectively, while the CARDO-O Rieske domain shows only 20.3% and 17.5% identities with the entire regions of BDO-F (a.a. 1–109) and CARDO-F (a.a. 4–107) (Figure 4(c)). While the directions of the regions between the two loops, which contain the ligands for the Rieske cluster, are identical between CARDO-O and the ferredoxins (Figure 4(c), red arrow), the sizes of the third walls (Figure 4(c), blue arrow), differ. As mentioned above, the third wall of the Rieske domain is considered to function as a stabilizer of head-to-tail contact between the α subunits. Since the ferredoxins exist as monomeric proteins, this difference may reflect differences in each quaternary structure.

Hydrogen bonds (H-bonds) around the Rieske cluster

The Fe1 atom of the Rieske cluster is co-ordinated by S^{γ} atoms of Cys69 and Cys90, whereas Fe2 is co-ordinated by $N^{\delta 1}$ atoms of His71 and His93

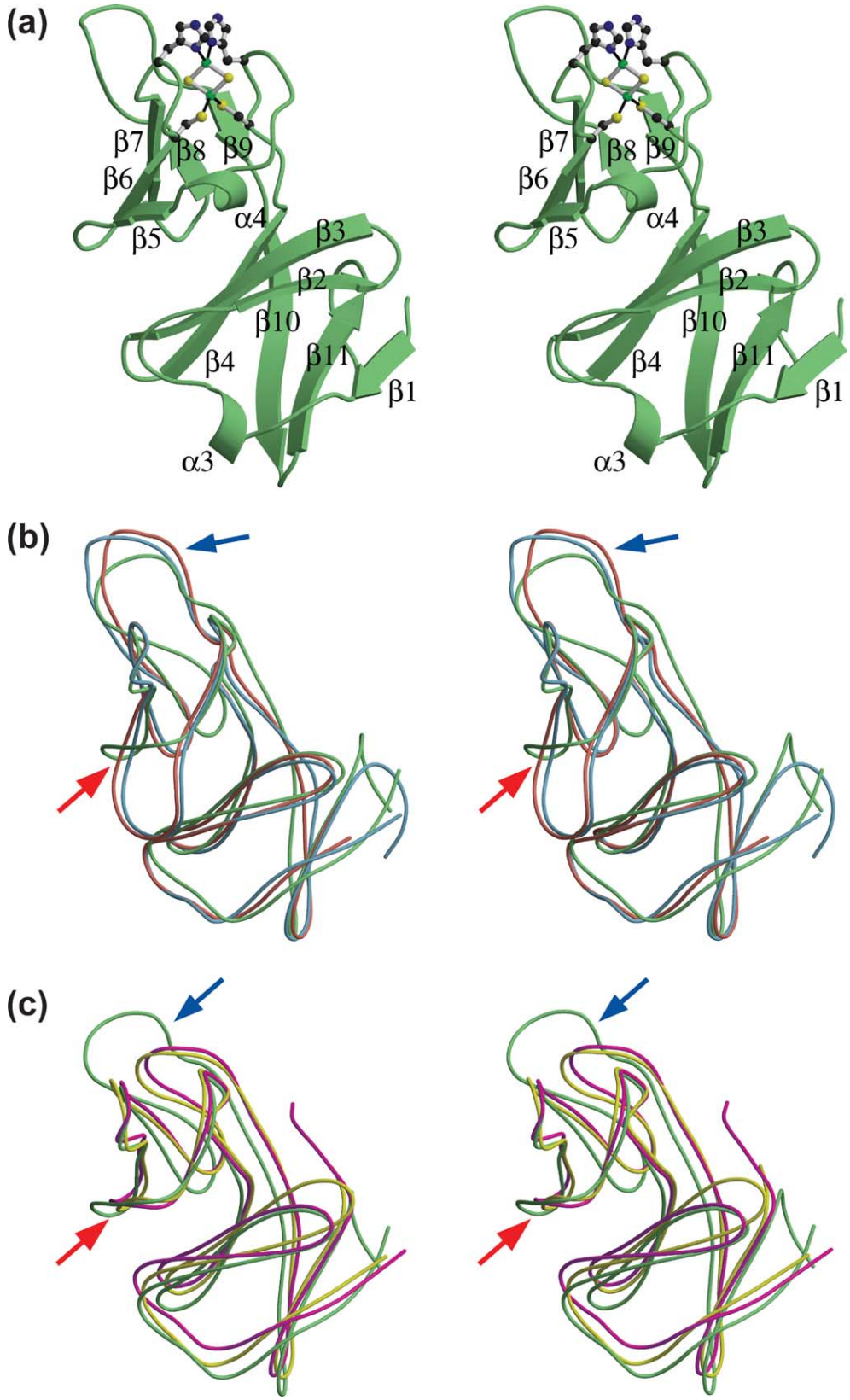

Figure 4. Structures of the Rieske domain of CARDO-O, with superimposition on the corresponding parts of the related proteins. (a) A stereoscopic ribbon structure of the Rieske domain of CARDO-O. The Rieske cluster and its ligands are shown by ball-and-stick models. (b) Stereoview of the superpositioning of the Rieske domains of the terminal oxygenases of three ROSs: CARDO-O (light-green), NDO-O (sky-blue), and BDO-O (salmon). In (c), the stereoview of the superpositioning of CARDO-O (light-green) and the Rieske-type ferredoxins, BDO-F (magenta) and CARDO-F (yellow), is shown. In (b) and (c), the positions of the regions between the two ligand-containing loops and the long loop, which constitutes the third wall at the tip of the Rieske domain, are shown by red and blue arrows, respectively.

(Figure 5(a)). There were H-bonds, i.e. bonds between the main-chain nitrogen of residue Arg72 to one of the cluster sulfides (S2), and the main-chain nitrogen atoms of residues His93 and Trp95 to the other cluster sulfide (S1). H-bonds were also observed between the S^{γ} atoms of the cysteinyl ligands Cys69 and Cys90 and the main-chain nitrogen atoms of His71 and Tyr92, respectively, (Figure 5(a)). Both $N^{\varepsilon 2}$ atoms of His71 and His93 were H-bonded to Asp359 $O^{\delta 2}$ and Asp180 $O^{\delta 2}$, respectively, although not illustrated in Figure 5(a). A similar H-bond network is also formed in the NDO-O structure (Figure 5(b)).

In higher redox potential Rieske cluster-containing proteins, such as mitochondrial cytochrome bc_1[17] (+300 mV) and chloroplast cytochrome b_6f[18] (+315 mV), two polar amino acid residues, which correspond to bc_1 residues Ser163 and Tyr165, were mostly conserved in the vicinity of the Rieske cluster. In the bc_1 structure, the side-chain atoms of the two residues, Ser163 O^{γ} and Tyr165 O^{η}, formed H-bonds with the cluster sulfide S1 and S^{γ} of the cysteinyl ligand (Cys139), respectively (Figure 5(d)). In the case of the CARDO-O structure, while the serine residue is replaced with Trp95, the tyrosine residue (Tyr97) is conserved, and Tyr97 O^{η} forms H-bond with S^{γ} of the first cysteinyl ligand (Cys69) (Figure 5(c)). On the other hand, while the two cluster-ligands-binding loops of the bc_1 fragment connect to each other *via* a disulfide bond, the two loops observed in CARDO-O are not connected covalently due to the replacement of the cysteine residues with Val74 and Tyr92 (Figure 5(c) and (d)). The loss of disulfide bonding between the two loops is a common feature among the known structures of the terminal oxygenases and ferredoxins of ROS, which constitute a class of the Rieske cluster-containing proteins with lower redox potential.

Previous studies have indicated that H-bond with the cluster is important in determining the redox potential of the electron transfer proteins.[19] Although the redox potential of the Rieske cluster

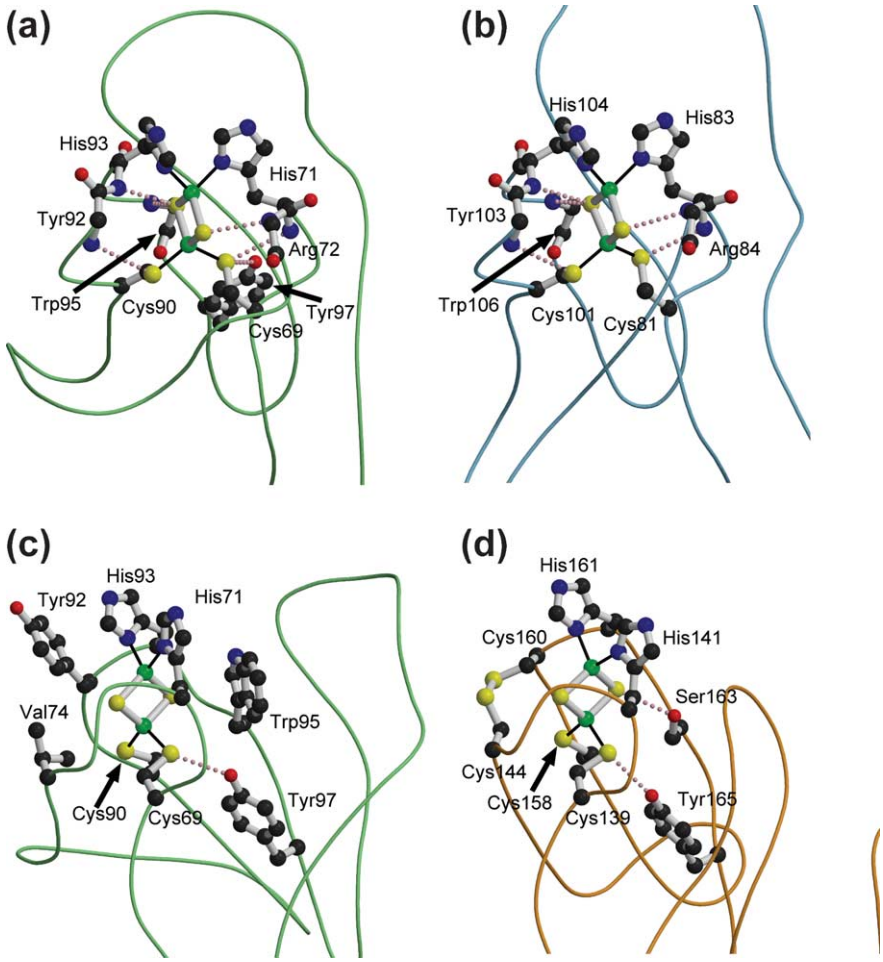

Figure 5. The network of H-bonds around the Rieske cluster of CARDO-O. (a) and (c) The structures of the Rieske cluster-flanking region of CARDO-O in the C^{α} backbone format. The view shown in (c) is rotated 90° about a vertical axis relative to the view in (a). (b) The structure of the Rieske cluster-flanking region of NDO-O in the same view as (a). (d) The structure of the Rieske cluster-flanking region of bovine bc_1 complex in the same view as (c). The Rieske cluster and its ligands, along with several surrounding a.a. residues are plotted as a ball-and-stick representation, and the Fe and S atoms are shown as green and yellow spheres, respectively. The H-bonds formed around the Rieske cluster are indicated by the pink broken lines.

in CARDO-O has not been measured, those of other terminal oxygenase components of ROSs, i.e. benzene dioxygenase and phthalate dioxygenase, have been reported as $-112(\pm 15)$ mV[20] and -150 mV,[21] respectively. The a.a. residues involved in the formation of H-bonds in the CARDO-O structure are completely conserved in the N-terminal half (roughly corresponding to the Rieske domain) of the phthalate dioxygenase oxygenase component (data not shown). Thus, it is reasonable to assume that the redox potential of CARDO-O is in the same range as that of phthalate dioxygenase oxygenase.

The catalytic domain

The catalytic domain is dominated by a seven-stranded antiparallel β-pleated sheet that extends into the middle of the domain of the CARDO-O subunit (Figure 3). The strand order is β12-22-21-20-19-16-15 from the interface between the Rieske and the catalytic domains to the bottom of the monomer molecule (Figure 3(b)). The sheet has tight connections between the strands on the side that packs against the Rieske domain, whereas all the insertions between the strands and C-terminal region are on the other side. The insertions between the strands and the C-terminal α-helix contain the ligands for mononuclear iron and form the active site pocket (Figure 3). The active site pocket is formed by four structural motifs, three of which are α-helices (α6, α7, and α11-3), and the remaining motif is a β-sheet. One side of the active site is formed by the long helix, α11, which is broken into three parts at a.a. 321–322 and a.a. 328–329, which loop out from the helix. The helix covers one part of the above-mentioned β-sheet in its full length. Asp333, which is a ligand for mononuclear iron at the active site, is located within the broken α11 helix (α11-3). The three helices, α6-8, cover the other side of the pocket between strands β12 and β13. The helix α7 contains an additional two ligands for mononuclear iron, His183 and His187. The conserved Asp180, which may provide the direct route for electron transfer, is located on the turn between the α6 and α7 helices.

Thus, the structure of the catalytic domain of CARDO-O is constructed by the sheet forming the base, with one broken helix packing against it and with other structural elements sticking out from the sheet against this helix. This structure is roughly similar to that of NDO-O, and the C^{α} folding of the entire catalytic domain of CARDO-O can be superimposed upon those of NDO-O with rmsd values of the C^{α} position of 13.1 Å (264 C^{α} atoms). However, there are three noteworthy differences between the two structures. The first difference is in the structure of the N-terminal part of the catalytic domain, which corresponds to residues 1–26 in CARDO-O and residues 1–37 in NDO-O. While only two α-helices are found in the CARDO-O structure, there are two β-strands (β1 and β2) and two α-helices in the NDO-O structure. In the case of the NDO-O structure, together with the β23 that is located within the long insertion of the β-sheet (between β22 and β24), both strands constitute a small sheet at the bottom of the molecule. The second difference lies in the C-terminal region, which is located after the long broken α-helix (α11-1 to α11-3). In the CARDO-O structure, there are three helices (α12, α13, and α14) within this region. Following α11-3, the C^{α} turns to the bottom of the molecule, and after helix α12, it turns back and extends towards the Rieske domain (Figure 3(b)). On the other hand, following the above-mentioned β23, there are two β- strands (β24 and β25), both of which are contained in the antiparallel β-sheet that is located in the middle of the catalytic domain of NDO-O, resulting in the nine-stranded β-sheet. Following the β25 strand, the C^{α} turns to the top of the NDO-O molecule, and after α11, turns back to the bottom of the molecule. The third difference concerns residues 239–251, which constitute the hook-like long loop structure between β16 and β19, which extends toward the bottom of the monomer molecule. This 13 a.a. long hook-like loop includes one β-strand (β18).

Co-ordination of iron at the active site

The mononuclear iron at the active site is co-ordinated by His183, His187, Asp333, and by a water molecule (Figure 6). The co-ordination geometry of the CARDO-O active site could be described as a distorted octahedral bipyramid with one ligand missing, as is seen for the active site of oxygenase components of ROSs.

In the NDO-O structure, the ligand histidine residues (His208 and His213) are H-bonded to the side-chains of aspartic acid residues (Asp205 and Asp361, respectively).[12] The corresponding histidine ligands in the CARDO-O structure are not bonded to aspartic acid, but are H-bonded to carbonylic oxygen in the main chain. The $N^{\varepsilon 2}$ of His183 H-bonds to the main-chain oxygen atoms of Asn177 and Asp180, and similarly His187 bonds to Phe329 (Figure 6).

Electron transfer from the Rieske cluster to the active site

Based on the CARDO-O structure, electron transport between the Rieske cluster and the non-heme iron of the neighboring subunit is considered to be mediated by Asp180. In the CARDO-O structure, as shown in Figure 6, a carboxylic oxygen of the side-chain of Asp180 binds to His93 of the neighboring subunit, which is a ligand for the Rieske cluster. Because the $O^{\delta 1}$ and $O^{\delta 2}$ atoms of Asp180 are rather distant from the $N^{\delta 1}$ of His183 (at distances of 4.7 Å and 5.3 Å, respectively) (Figure 6), H-bonds are probably not formed between these atoms. Since the $N^{\delta 1}$ in His183 forms an H-bond to the main-chain carbonyl group of Asp180, the electron transfer pathway between the CARDO-O subunits can be proposed as follows: from the

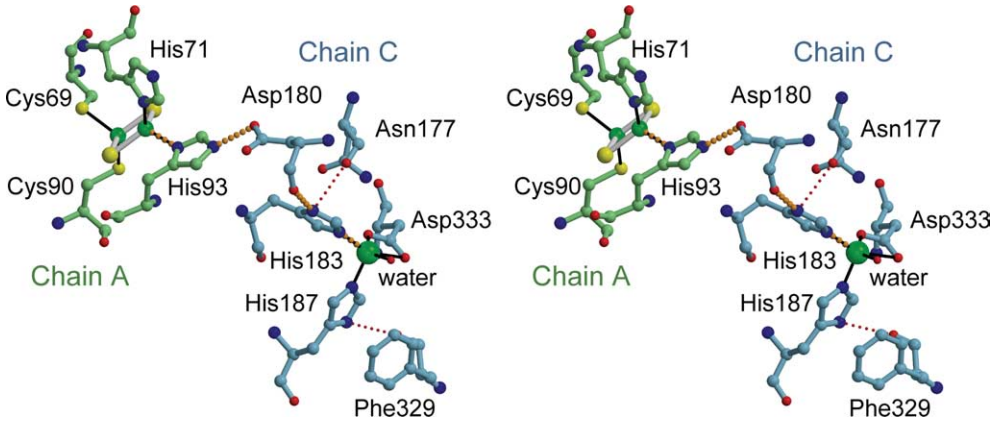

Figure 6. Stereoview of the iron co-ordination at the active site of CARDO-O, and the proposed electron transport pathway from the Rieske cluster of the adjacent subunit. Chain A, which has a Rieske cluster, and chain C, which has an active site iron, are distinguished by the bonds that are colored light green and sky-blue, respectively. The orange broken lines indicate the proposed electron transport pathway. The Rieske cluster is plotted as a ball-and-stick rhombus, and the iron ions, sulfides, and the ligand-bonded water molecule are shown as green, yellow, and small red spheres, respectively. H-bonds between the histidine ligands of iron and the backbone nitrogen atoms of the surrounding a.a. residues are shown as red, broken, thin lines.

imidazole $N^{\varepsilon 2}$ atom of the His93 ligand for the Rieske cluster to the $O^{\delta 2}$ of Asp180 (distance of 2.6 Å), then to the imidazole $N^{\delta 1}$ atom of the active site ligand His183 *via* the amide group of Asp180 (2.5 Å), and finally, to the non-heme iron in the active site (Figure 6). Based on the recent coordinates of NDO-O (Protein Data Bank accession code, 1O7G), a similar electron transfer pathway, which is mediated by Asp205, was proposed for NDO-O.[22]

Interactions between the subunits

When the two subunits of CARDO-O interact in the head-to-tail manner, 13 H-bonds and many non-bonded interactions are formed (Figure 7(a)). The interface between CARDO-O subunits consists of 54 residues and the accessible area buried in the interface is about 2300 $Å^2$ for each subunit, which was calculated by the program GRASP.[23] The area buried constitutes 15% of the total surface areas of a single subunit. Meanwhile, in the NDO-O structure, the α subunits interface consists of 54 residues that constitute 15 H-bonds and formed buried area with approximately 2700 $Å^2$ for each subunit (17% of the total surface areas). These results suggested that only the differences in interface area and the number of H-bonds formed cannot explain the difference in their tertiary structures. However, there is a hook-like long loop at the bottom of the catalytic domain in the CARDO-O structure (Figure 7(a)). Although this region corresponds to the insertion in the β-sheet (between β18 and β19) in the NDO-O structure, a similar loop structure is not formed (Figure 7(b)). When the two CARDO-O subunits interact, one H-bond and non-bonded interactions are formed between this hook-like long loop in the catalytic domain and the long loop in the Rieske domain of the neighboring subunit (Figure 7(a)). In detail, Gly244 in the hook-like long loop H-bonds to Asp106 in the Rieske domain, and two hydrophobic residues (Ile243 and Val248) in the hook-like long loop make hydrophobic interactions with Leu108 in the Rieske domain. The structures of the regions between the two ligand-containing loops are also markedly different in CARDO-O and NDO-O. In the NDO-O structure, this region constitutes the loop and is localized close to the catalytic domain of its own α subunit; the corresponding region in CARDO-O lies close to its own Rieske cluster and neighboring catalytic domain (Figure 4(b)). Due to these structural differences, the corresponding part (α4 helix) of the CARDO-O can interact with the α11-3 of the neighboring α subunit (Figure 7(a)) by the hydrophobic interaction (between Val78 and Trp335) and several H-bond networks *via* water molecules. However, in the NDO-O, it interacts with the loop between β1 and β2 of the neighboring β subunit (Figure 7(b)). In addition, Trp91, Tyr92 and Trp95 in the Rieske domain form hydrophobic interactions with Tyr185, Ile186, Trp335, Ile354 and Phe356 in the catalytic domain.

In the CARDO-O structure, the above structures may contribute, in the main, to the stabilization of the appropriate interaction between the α subunits for the effective transfer of electrons, in contrast to the β subunit of terminal oxygenases, which have the $\alpha_3\beta_3$ configuration, as is the case with NDO-O. As the result of the alignment analyses between the a.a. sequences of CARDO-O_{J3} subunit ($CarAa_{J3}$) and other oxygenase components of class IA ROSs including phthalate dioxygenase, which is reported to have the terminal oxygenase component with α_4 or α_6 configurations,[8] we could not clearly identify the regions corresponding to those that contribute to stabilize the α_3 configuration of CARDO-O (data not shown). Therefore, the above subunit interaction might be specific for the CARDO-O

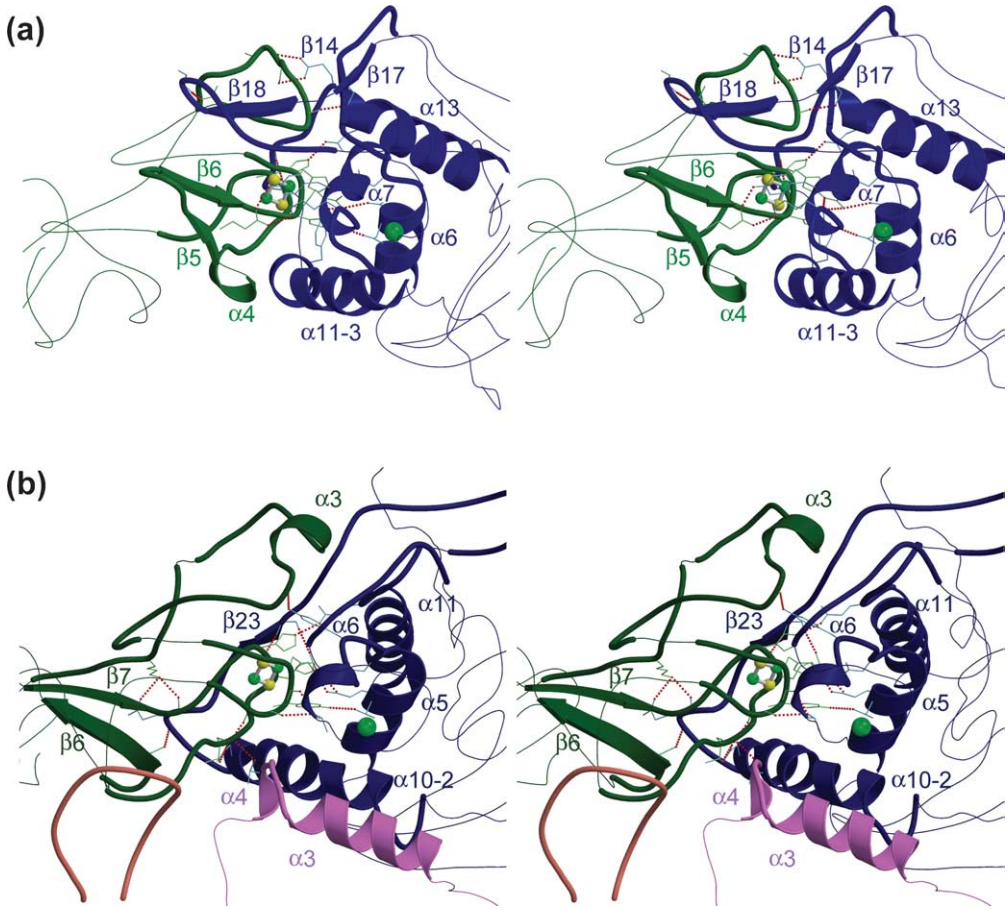

Figure 7. Comparison of the subunit interactions between CARDO-O and NDO-O. Stereoview of the interfaces between the subunits of CARDO-O (a) and NDO-O (b) is shown. The α-subunits are colored (a) forest-green and blue or (b) dark-green and dark-blue. In (b), the β-subunits are colored magenta and orange. Regions that are involved in subunit H-bonding or non-bonded interactions are emphasized. H-bonds formed between the subunits are indicated by red broken lines. The Rieske cluster and an active site iron are shown in a ball-and-stick rhombus or a CPK model representation, and the iron and sulfide ions are colored green and yellow, respectively.

structure. To clarify this speculation, the structural analysis of other terminal oxygenase components of ROSs, which consist of only catalytic subunits, is necessary.

Substrate-binding pocket

The active site iron is positioned approximately 18 Å from the surface of the CARDO-O molecule (Figure 8(a) and (b)). From the surface, a cavity provides the substrate with access to the active site iron. The entrance of this cavity consists of the α10 helix, β17 strand, and a loop between the β18 and β19 strands; the CARDO-O cavity is larger than that of NDO. The wall of the cavity is formed by three helices (α6, α7, and α11-3), and the β-sheet located at the middle of the catalytic domain.

The shape of the substrate-binding pocket of CARDO-O (Figure 8(b)) is quite different from that of NDO-O. The cavity is divided into two regions, which are proximal and distal to the entrance (designated as the P and D-regions, respectively), by the active site iron. The P-region consists primarily of hydrophobic residues, as does the corresponding region of NDO-O, and the size is approximately 8 Å × 11 Å × 18 Å. This region contains two iron-ligand histidine residues, as well as the hydrophobic residues, Ile184, Ile186, Phe275, and Phe329 occupying positions near the active site iron. This hydrophobic environment around the substrate-binding pocket seems reasonable, since the enzyme prefers aromatic compounds as its primary substrates. The D-region is made into a forked shape by Glu284 and is narrower than the P-region, with a width of about 5 Å and a depth of 5 Å. Hydrophobic residues (Leu270, Val 272 and Ile334) are included in the D-region, although there are also many polar residues (Gln282, Glu284, Tyr286, Tyr296, Asn330, Arg337 and the iron-ligand Asp333) in this region. Compared to the other related enzymes, the presence of polar residues in the D-region is an important and unusual characteristic of CARDO-O, and may be related to its origin.

Superimposition of the residues located 10 Å from the active site iron in CARDO-O with those in NDO-O is shown in Figure 8(c). Although the three iron ligands and neighboring Asp residues

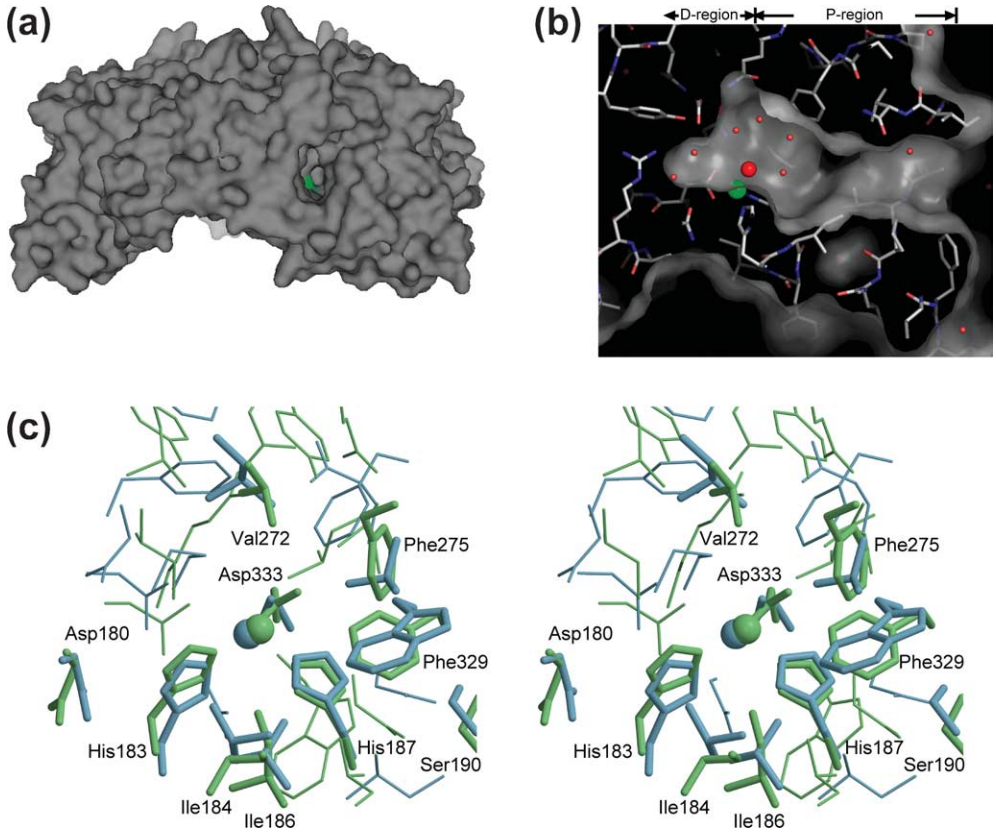

Figure 8. The substrate-binding pocket of CARDO-O. (a) The surface plot of CARDO-O. The view shown in (a) is almost identical with that shown in Figure 2(b). A long cavity leads from the surface of the molecule to the active site iron (green). (b) The molecular surfaces of the long cavity of CARDO-O. The water molecule ligand-bound to the active site iron (shown in the CPK model and colored green) and other water molecules are shown as large and small red spheres, respectively. In (c), the stereoview of the superposition of the residues located at <10 Å from the active site iron in CARDO-O (light green) and NDO-O (sky-blue) is shown. The side-chains of the residues that form the substrate-binding pocket are shown in the wire-frame model, and the catalytic mononuclear irons are shown in the CPK model. The ligands for the active site iron (His183, His187, and Asp 333), Asp180, Ile184, Ile186, Ser190, Val272, Phe275, and Phe329 in CARDO-O are labeled and emphasized. The residues in NDO-O that correspond to the ten residues in CARDO-O are also emphasized.

that are probably involved in electron transport can be roughly superimposed, the remaining residues that form the wall of the substrate-binding pocket cannot be superimposed for these two enzymes.

Substrate specificity of CARDO-O interpreted by docking simulation

In order to deduce the mechanism of the reaction specificity of CARDO-O from the shape and physicochemical property of the substrate-binding pocket, we performed docking simulations of CAR. The predicted docking structures could be grouped into two clusters. The rmsd values of non-hydrogen atoms of the members of each cluster from its cluster center were less than 0.5 Å, and the rmsd values between structures from different clusters were about 1 Å. The representative structures of both clusters are shown in Figure 9(a) and (b). Both binding conformations are stabilized by H-bonding between the imino nitrogen and the carbonyl oxygen of Gly178. Among the carbon atoms of the substrate, those at the angular (C9a) and its adjacent (C1) positions are closest to the oxygen atoms (O1 and O2, respectively) in both conformations. In all the predicted docking structures, the distances between C9a and O1 and between C1 and O2 are 3.07($\pm$0.05) Å and 2.84($\pm$0.08) Å, respectively. This binding manner agrees with the fact that CARDO-O catalyzes the angular dioxygenation for CAR. Note that the simulated docking structures were converged on either of the two binding conformations, even when the distance restraints were imposed on the carbon atoms at the lateral positions. Therefore, the distance restraints used here did not bias the distribution of the docking structures. Such distances between the oxygen atoms and the carbon atoms attacked in the docking models are comparable to those reported for the NDO-O:dioxygen:indole ternary complex.[22] This suggests that the mechanism of dioxygenation of CARDO-O is the same as that of NDO-O. The difference in the sites attacked is thus attributed to the difference in the binding conformations of the substrates, which, in turn, arises from the difference in the shapes and

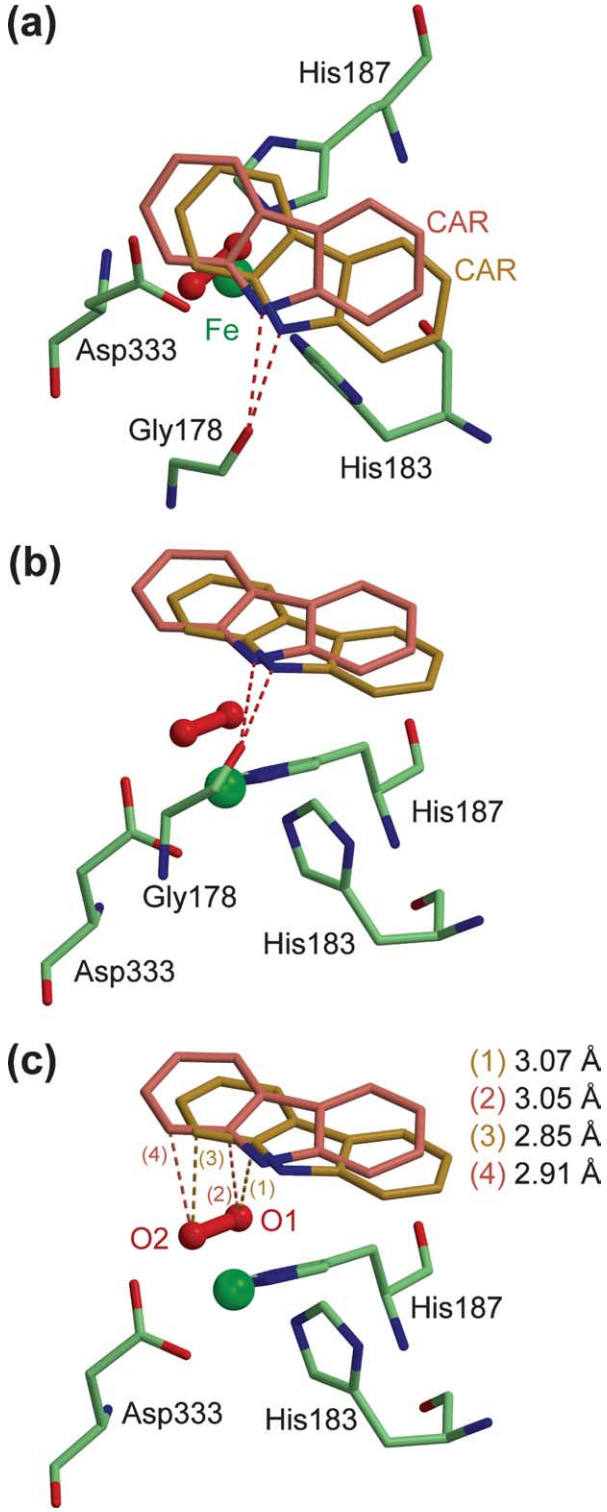

Figure 9. Computer-predicted docking structures of CAR in the CARDO-O active site. (a) and (b) Two representative binding conformations of CAR to dioxygen-bound CARDO-O. Two models of CAR are colored salmon and golden rod, and H-bonds formed between the imino nitrogen of CAR and main-chain oxygen of Gly178 are indicated by red broken lines. The ligands for the active site iron (His183, His187, and Asp 333) are shown in the wire-frame model, and the catalytic mononuclear irons are shown in the CPK model (green). The modeled dioxygen-bound active site of CARDO-O is shown by ball-and-stick models (red). In (c), the distances between C9a and O1, and between C1 and O2 in the two representative binding conformations are shown.

physicochemical properties of the substrate-binding pockets of CARDO-O and NDO-O.

To clarify the molecular mechanism underlying the catalysis of other unique reactions,[6] it will be necessary to determine the binding positions of other various substrates. In addition to the *in silico* analysis, the determination of CARDO-O:substrate complex and CARDO-O:substrate:dioxygen ternary complex structures by X-ray crystallography will also be important. Furthermore, to improve the applicability of CARDO for bioremediation of dioxin contamination, the structure-based interpretation of the low capability of CARDO-O to oxygenate highly chlorinated dioxin congeners will be important.

Possible binding site with CARDO-F

Considering that the interactions between α subunits are roughly conserved between CARDO-O and NDO-O (Figure 2), it seems likely that these two terminal oxygenases interact with their respective ferredoxins in similar manners. Since, in NDO-O, the interface between the α and β subunits is blocked from interacting with the ferredoxin molecule, CARDO-F is believed to contact CARDO-O at the top or side of the molecule. As shown in Figure 10, there are two pronounced depressions around each subunit interface. One of the depressions is positively charged, and the other is negatively charged. Considering that the Rieske cluster of CARDO-O locates inside the negatively charged depression, we assume CARDO-F binds to this region in CARDO-O. If it is the case, the distance between two Rieske clusters is about 15–20 Å, whose distance is reasonable in the electron transfer from CARDO-F to CARDO-O.

Materials and Methods

Expression of His-tagged form of CARDO-O

In order to express the CARDO-O_{J3} in the C-terminal-histidine-tagged form, we used the pET-26b(+) vector (Novagen, Madison, WI). Artificial NdeI and XhoI sites were created at the 5′ and 3′-ends of the *carAa* gene, respectively, by PCR using template DNA (pBJ3001)[15] and the following primer set: 5′-*CATATG*GCGAACGTTG ATGAGGCAAT-3′ and 5′-*CTCGAG*GCCCGAAACGTG CGCTTGGGTCTGAATACCCTG-3′ (NdeI and XhoI restriction sites italicized). The resultant PCR amplicon was ligated into the NdeI and XhoI sites of pET-26b(+), to produce pEJ3AaC.

E. coli strain BL21(DE3) (Novagen) harboring pEJ3AaC was grown in Luria-Bertani (LB) medium[24] or SB medium[4] that was supplemented with kanamycin (50 μg/ml) at 37 °C for the initial incubation and at 25 °C for the induction of protein expression with shaking at 120 rpm. When the absorbance at 600 nm reached approximately 0.5, 0.5 mM isopropyl-β-D-thiogalactopyranoside (IPTG) was added. After 15 hours incubation with IPTG, the *E. coli* cells were harvested by centrifugation. The SeMet substituent of CARDO-O_{J3} was expressed in the *E. coli* methionine auxotroph strain

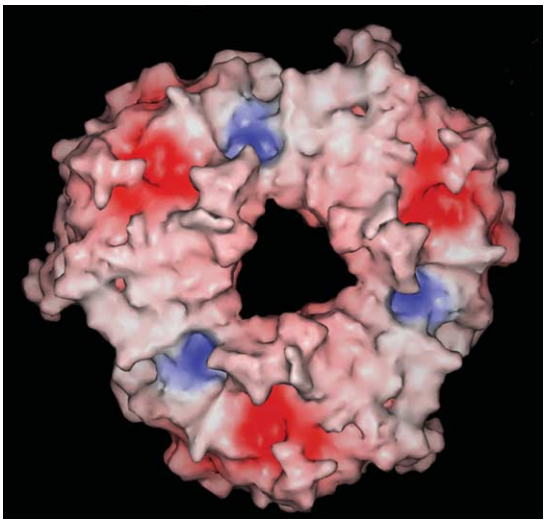

Figure 10. Surface electrostatic potentials and overall shapes of CARDO-O. The view along the molecular 3-fold axis, which is identical with that shown in Figure 2(a), is shown. The negatively charged surface is colored red, and the positively charged surface is colored blue.

B834 (DE3) (Novagen). *E. coli* strain B834 (DE3) (pEJ3AaC) was grown in medium that contained SeMet[25] and harvested by centrifugation.

Preparation of purified CARDO-O

All of the purification procedures were carried out at 4 °C. Appropriate *E. coli* cells were suspended in TI buffer (20 mM Tris–HCl (pH 7.5), 60 mM imidazole, 0.5 M NaCl). The crude cell extract, which was prepared by sonication and subsequent centrifugation, was applied to a HiTrap Chelating HP column (Amersham Biosciences, Tokyo, Japan) according to the manufacturer's recommendation. After sodium dodecyl sulfate-polyacrylamide gel electrophoresis (SDS-PAGE), the fractions that contained CARDO-O_{J3} were pooled and concentrated by ultrafiltration using Centriprep-10 (Millipore, Bedford, MA). The resultant preparation was further purified by gel-filtration chromatography (GFC) using a Superdex 200 column (26 mm × 600 mm; Amersham Biosciences) and GFC buffer (20 mM Tris–HCl (pH 7.5), 0.2 M NaCl, 10% (v/v) glycerol). Fractions that contained CARDO-O_{J3} were concentrated, and buffer-exchanged with the 5 mM Tris–HCl buffer (pH 7.5) for the crystallization experiments.

Analytical methods

To determine the CAR-oxygenating activity of the CARDO-O after the purification from crude cell extract and after the crystallization, *in vitro* reconstitution assays were performed: 1 ml of the reaction mixture (50 mM Tris–HCl (pH7.5)) contained 100 nmol NADH, 1 nmol FAD, 100 nmol $Fe(SO_4)_2(NH_4)_2$, 0.8 mg of crude cell protein of *E. coli* JM109 harboring pUCA14[3] expressing both CARDO-F and CARDO-R, and 100 μg of the purified or the dissolved CARDO-O protein. The reaction was initiated by adding 60 nmol of CAR dissolved in 1 μl of dimethyl sulfoxide. After incubation for two hours at 30 °C, the reaction was stopped by putting into ice. The products were extracted with 2 ml of ethyl acetate, and then applied to gas chromatography-mass spectrometry to quantify the product formed as described.[6] The iron content of the dissolved crystal of CARDO-O was determined by iron-chelating reagent Feren S as described.[4]

Crystallization and data collection

The initial crystallization trials of CARDO-O_{J3} were carried out using the reservoirs from several commercially available crystallization kits. The final crystallization conditions for CARDO-O_{J3} crystals were as follows: 15–17.5% (±)-2-methyl-2,4-pentanediol (MPD), 0.1 M Mes (pH 6.2), and 15–25 mg/ml protein at 20 °C. After incubation for two to three days, the cubic-form crystal was grown by hanging-drop, vapor-diffusion (1:1 (v/v) ratio of precipitating solution to protein). The X-ray diffraction data for the non-substituted CARDO-O_{J3} crystals were collected at 100 K on the BL41XU station of SPring-8 at the Japan Synchrotron Radiation Research Institute (JASRI). The diffraction data were processed with the HKL2000 software.[26] The data collection and processing statistics are given in Table 1.

MAD phasing

The CARDO-O_{J3} protein structure was determined from the three-wavelength MAD experiment (peak 0.9794 Å; edge 0.9796 Å; and remote 0.9820 Å) using the anomalous scattering of Se in the SeMet-substituted protein (Table 1). The collected data were processed and scaled using DPS/MOSFLM.[27] The phase calculation was performed by the Solve/Resolve program.[28,29] The positions of the six high peaks of Se (six Se/one molecule per asymmetric unit) were determined at 2.3 Å (FOM is 0.38). Density modification of the phase from the Solve program was performed in DM in CCP4,[30] using solvent flattening and histogram matching. After DM, the electron density map was clearly interpretable.

Structure refinement

The ARP/wARP program[31] in CCP4 was applied to the modified phase in combination with the 1.95 Å diffraction data from the native crystal, for the initial model building. The auto main-chain tracing routine produced five polypeptide fragments (375 residues, 96%) and a connectivity index of 0.97. Model rebuilding and refinement in the electron density map was carried out with the QUANTA (Accelrys, San Diego, CA) and Xtalview[32] programs. Refinement was carried out using the Refmac5 programs in CCP4 and CNS 1.1,[33] by gradually adding water molecules. The stereochemistry of the model was analyzed using the PROCHECK[34] and WHATCHECK[35] programs. The refinement statistics are listed in Table 1. The Figures were generated using MOLSCRIPT,[36] Raster3D,[37] and PyMOL.[38]

Structural comparisons were performed with the QUANTA program. H-bonding and hydrophobic interactions within the protein structures were predicted using the LIGPLOT program.[39] The area buried in the subunit interface was calculated by the program GRASP.[23] Calculation and drawing of the surface electronic potentials were carried out with the SPOCK program.[40]

Docking simulation between CAR and the substrate-binding pocket of CARDO-O

The structure of the CARDO:dioxygen:CAR ternary complex was modeled as follows. The position of the dioxygen was calculated, based on the assumption that the dioxygen binds to the mononuclear iron at the active site of CARDO-O in a manner similar to that observed in the NDO-O:dioxygen complex. The coordinates of the NDO-O:dioxygen:indole complex[22] (Protein Data Bank accession code 1O7N) were translated and rotated to minimize the rmsd value between the active center atoms. The obtained positions of the oxygen atoms were used as those in the CARDO-O active site.

The docking simulation of CAR to the active site of CARDO-O was performed by using GOLD version 2.1.[41] The search area was a sphere with a radius of 10 Å centered at the active center position near the mononuclear iron determined by Pass version 1.1.[42] During the docking simulation, harmonic distance restraints were imposed between the dioxygen and the carbon atoms at the reaction sites of the substrate, when the distance was greater than 3.5 Å. All possible reaction sites, i.e. one angular (C1–C9a), and two lateral (C1–C2 and C3–C4) positions were tested and ten independent simulations were executed for each condition. All of the predicted docking structures were classified into clusters using rmsd values between non-hydrogen atoms of the substrate as a distance measure.

Protein Data Bank accession number

The co-ordinates for the structure of CARDO-O have been deposited in the RCSB Protein Data Bank with accession code 1WW9.

Acknowledgements

We thank the staff of the Photon Factory and SPring-8 for data collection, and Dr Fushinobu of The University of Tokyo for helpful comments. The data collection was approved by the Photon Factory Advisory Committee (Proposal number 03G124), and the JASRI (Proposal number 2003A0124-NL1-np). This work was supported by the Program for Promotion of Basic Research Activities for Biosciences (PROBRAIN), and SBSP (Structural Biology Sakabe Project).

Supplementary Data

Supplementary data associated with this article can be found, in the online version, at doi:10.1016/j.jmb.2005.05.059

References

1. Arcos, J. C. & Argus, M. F. (1968). Molecular geometry and carcinogenic activity of aromatic compounds. New perspectives. *Advan. Cancer Res.* **11**, 305–471.
2. Nojiri, H. & Omori, T. (2002). Molecular bases of aerobic bacterial degradation of dioxins: involvement of angular dioxygenation. *Biosci. Biotechnol. Biochem.* **66**, 2001–2016.
3. Sato, S., Nam, J.-W., Kasuga, K., Nojiri, H., Yamane, H. & Omori, T. (1997). Identification and characterization of gene encoding carbazole 1,9a-dioxygenase in *Pseudomonas* sp. strain CA10. *J. Bacteriol.* **179**, 4850–4858.
4. Nam, J.-W., Nojiri, H., Noguchi, H., Uchimura, H., Yoshida, T., Habe, H. *et al*. (2002). Purification and characterization of carbazole 1,9a-dioxygenase, a three-component dioxygenase system of *Pseudomonas resinovorans* strain CA10. *Appl. Environ. Microbiol.* **68**, 5882–5890.
5. Resnick, S. M., Lee, K. & Gibson, D. T. (1996). Diverse reactions catalyzed by naphthalene dioxygenase from *Pseudomonas* sp strain 9816. *J. Ind. Microbiol.* **17**, 438–457.
6. Nojiri, H., Nam, J.-W., Kosaka, M., Morii, K., Takemura, T., Furihata, K. *et al*. (1999). Diverse oxygenation catalyzed by carbazole 1,9a-dioxygenase from *Pseudomonas* sp. strain CA10. *J. Bacteriol.* **181**, 3105–3113.
7. Batie, C. J., Ballou, D. P. & Correll, C. C. (1991). Phthalate dioxygenase reductase and related flavin-iron-sulfur containing electron transferases. In *Chemistry and Biochemistry of Flavoenzymes* (Muller, F., ed.), vol. 3, pp. 543–556, CRC Press, Boca Raton, FL.
8. Tarasev, M., Rhames, F. & Ballou, D. P. (2004). Rates of phthalate dioxygenase reaction with oxygen are dramatically increased by interactions with phthalate and phthalate oxygenase reductase. *Biochemistry*, **43**, 12799–12808.
9. Mason, J. R. & Cammack, R. (1992). The electron-transport proteins of hydroxylating bacterial dioxygenases. *Annu. Rev. Microbiol.* **46**, 277–305.
10. Nam, J.-W., Noguchi, H., Fujimoto, Z., Mizuno, H., Ashikawa, Y., Abo, M. *et al*. (2005). Crystal structure of the ferredoxin component of carbazole 1,9a-dioxygenase of *Pseudomonas resinovorans* strain CA10, a novel Rieske non-heme iron oxygenase system. *Proteins: Struct. Funct. Genet.* **58**, 779–789.
11. Nam, J.-W., Fujimoto, Z., Mizuno, H., Yamane, H., Yoshida, T., Habe, H. *et al*. (2002). Crystallization and preliminary crystallographic analysis of the terminal oxygenase component of carbazole 1,9a-dioxygenase of *Pseudomonas* strain CA10. *Acta Crystallog. sect. D*, **58**, 1350–1352.
12. Kauppi, B., Lee, K., Carredano, E., Parales, R. E., Gibson, D. T., Eklund, H. & Ramaswamy, S. (1998). Structure of an aromatic-ring-hydroxylating dioxygenase-naphthalene 1,2-dioxygenase. *Structure*, **6**, 571–586.
13. Furusawa, Y., Nagarajan, V., Tanokura, M., Masai, E., Fukuda, M. & Senda, T. (2004). Crystal structure of the terminal oxygenase component of biphenyl dioxygenase derived from *Rhodococcus* sp. strain RHA1. *J. Mol. Biol.* **342**, 1041–1052.
14. Dong, X., Fushinobu, S., Fukuda, E., Terada, T., Nakamura, S., Shimizu, K. *et al*. (2005). Crystal structure of the terminal oxygenase component of cumene dioxygenase from *Pseudomonas fluorescens* IP01. *J. Bacteriol.* **187**, 2483–2490.
15. Inoue, K., Widada, J., Nakai, S., Endoh, T., Urata, M., Ashikawa, Y. *et al*. (2004). Divergent structures of carbazole degradative *car* operons isolated from Gram-negative bacteria. *Biosci. Biotechnol. Biochem.* **68**, 1467–1480.
16. Colbert, C. L., Couture, M. M.-J., Eltis, L. D. & Bolin, J.

T. (2000). A cluster exposed: structure of the Rieske ferredoxin from biphenyl dioxygenase and the redox properties of Rieske Fe-S protein. *Structure*, **8**, 1267–1278.
17. Iwata, S., Saynovits, M., Link, T. A. & Michel, H. (1996). Structure of a water soluble fragment of the "Rieske" iron-sulfur protein of the bovine heart mitochondrial cytochrome bc_1 complex determined by MAD phasing at 1.5 Å resolution. *Structure*, **4**, 567–579.
18. Carrell, C. J., Zhang, H., Cramer, W. A. & Smith, J. L. (1997). Biological identity and diversity in photosynthesis and respiration: structure of the lumen-side domain of the chloroplast Rieske protein. *Structure*, **5**, 1613–1625.
19. Hunsicker-Wang, L. M., Heine, A., Chen, Y., Luna, E. P., Todaro, T., Zhang, Y. M. *et al*. (2003). High-resolution structure of the soluble, respiratory-type Rieske protein from *Thermus thermophilus*: analysis and comparison. *Biochemistry*, **42**, 7303–7317.
20. Geary, P. J., Saboowalla, F., Patil, D. & Cammack, R. (1984). An investigation of the iron-sulphur proteins of benzene dioxygenase from *Pseudomonas putida* by electron-spin-resonance spectroscopy. *Biochem. J.* **217**, 667–673.
21. Gassner, G. T., Ludwig, M. L., Gatti, D. L., Correl, C. C. & Ballou, D. P. (1995). Structure and mechanism of the iron-sulfur flavoprotein phthalate dioxygenase reductase. *FASEB J.* **9**, 1411–1418.
22. Karlsson, A., Parales, J. V., Parales, R. E., Gibson, D. T., Eklund, H. & Ramaswamy, S. (2003). Crystal structure of naphthalene dioxygenase: side-on binding of dioxygen to iron. *Science*, **299**, 1039–1042.
23. Nicholls, A., Sharp, K. A. & Honig, B. (1991). Protein folding and association-insights from the interfacial and thermodynamic properties of hydrocarbons. *Proteins: Struct. Funct. Genet.* **11**, 281–296.
24. Sambrook, J. & Russell, D. W. (2001). *Molecular Cloning. A Laboratory Manual*, 3rd edit., Cold Spring Harbor Laboratory Press, Cold Spring Harbor, NY.
25. Doublie, S. & Carter, J. C. W. (1992). Preparation of selenomethionyl protein crystals. In *Crystallization of Nucleic Acids and Proteins: A Practical Approach* (Ducruix, A. & Giege, R., eds), pp. 311–317, Oxford University Press, New York, NY.
26. Otwinowski, Z. & Minor, W. (1997). Processing of X-ray diffraction data collected in oscillation mode. *Methods Enzymol.* **276**, 307–326.
27. Rossmann, M. G. & van Beek, C. G. (1999). Data processing. *Acta Crystallog. sect. D*, **55**, 1631–1640.
28. Terwilliger, T. C. (2000). Maximum likelihood density modification. *Acta Crystallog. sect. D*, **56**, 965–972.
29. Terwilliger, T. C. & Berendzen, J. (1999). Automated MAD and MIR structure solution. *Acta Crystallog. sect. D*, **55**, 849–861.
30. Collaborative Computational Project, Number 4. (1994). The CCP4 suite: programs for protein crystallography. *Acta Crystallog. sect. D*, **50**, 760–763.
31. Lamzin, V. S. & Wilson, K. S. (1993). Automated refinement of protein models. *Acta Crystallog. sect. D*, **49**, 129–147.
32. McRee, D. E. (1999). XtalView/Xfit: a versatile program for manipulating atomic coordinates and electron density. *J. Struct. Biol.* **125**, 156–165.
33. Brünger, A. D., Adams, P. D., Clore, G. M., DeLano, W. L., Gros, P. & Grosse-Kunstleve, R. W. (1998). Crystallography and NMR system: a new software suite for macromolecular structure determination. *Acta Crystallog. sect. D*, **54**, 905–921.
34. Laskowski, R. A., MacArthur, M. W., Moss, D. S. & Thornton, J. M. (1992). *PROCHECK v.2.: Programs to Check the Stereochemistrial Quality of Protein Structures*, Oxford Molecular Ltd, Oxford, UK.
35. Hooft, R. W. W., Vriend, G., Sander, C. & Abola, E. E. (1996). Errors in protein structures. *Nature*, **381**, 272.
36. Kraulis, P. J. (1991). MOLSCRIPT: a program to produce both detailed and schematic plots of protein structures. *J. Appl. Crystallog.* **24**, 946–950.
37. Merritt, E. E. & Bacon, D. J. (1997). Raster3D: photorealistic molecular graphics. *Methods Enzymol.* **277**, 505–524.
38. DeLano, W. L. (2001). *The PyMOL User's Manual*, DeLano Scientific, San Carlos, CA.
39. Wallace, A. C., Lakowski, R. A. & Thornton, J. M. (1995). LIGPLOT: A program to generate schematic diagrams of protein–ligand interactions. *Protein Eng.* **8**, 127–134.
40. Christopher, J. A. & Baldwin, T. O. (1998). SPOCK: real-time collaborative molecular modeling. *J. Mol. Graph. Model.* **16**, 285.
41. Jones, G. & Glen, C. R. (1995). Molecular recognition of receptor sites using a genetic algorithm with a description of desolvation. *J. Mol. Biol.* **245**, 43–53.
42. Brady, G. P., Jr & Stouten, W. F. P. (2000). Fast prediction and visualization of protein binding pockets with PASS. *J. Comput. Aided Mol. Des.* **14**, 383–401.

Edited by R. Huber

(Received 7 February 2005; received in revised form 24 May 2005; accepted 25 May 2005)

Available online 27 June 2005